Journal of Computational Physics **152,** 78–101 (1999)
Article ID jcph.1999.6235, available online at http://www.idealibrary.com on IDEAL®

# Development of an Implicit Method for Multi-fluid Flow Simulations

R. F. Kunz,*,[1] W. K. Cope,* and S. Venkateswaran†

*Lockheed Martin, Schenectady, New York 12301; and †University of Tennessee Space Institute, Tullahoma, Tennessee 37388

Received August 27, 1998; revised February 8, 1999

A fully coupled implicit method has been developed for solving the viscous full multi-fluid equations, which incorporate transport and generation of mass and momentum for each component present in a system. This work presents stability analysis and representative computational results of this algorithm. The stability analyses demonstrate the performance of several iterative schemes applied to the solution of the linearized block system which arises in the fully implicit formulation. These include block Jacobi and symmetric block Gauss–Siedel schemes using two forms of relaxation. A hierarchy of increasing physical complexity is pursued, starting with one-dimensional, two-fluid systems with minimum inter-field dynamic coupling and no mass transfer. These analyses are then extended to systems employing physically important inter-field forces (drag, dispersion, virtual mass). The effects of mass transfer, multiple fields (i.e., more than 2), and multiple dimensions are considered. A two-fluid Navier–Stokes code has been developed, guided by the stability analyses. One-dimensional and two-dimensional results generated with this code are presented, which verify the validity of the stability analyses presented for the coupled scheme, and the effectiveness of the method for flows of engineering relevance. 

## INTRODUCTION

Multi-phase flows which require full multi-fluid modeling arise in a wide class of engineering problems, where non-equilibrium dynamics and thermodynamics of the interfaces between constituents play important roles in the evolution of the mean flow. Examples include cyclone separators, two-phase flow in jets and curved ducts, and boiling flow in heat exchangers. Such flows contrast with multi-phase flows where interfacial dynamics and

[1] To whom correspondence should be addressed at current address: Applied Research Laboratory, Garfield Thomas Water Tunnel—3rd Floor, The Pennsylvania State University, University Park, PA 16802. E-mail: rfk102@psu.edu.



0021-9991/99 $30.00

thermodynamics occur on such small scales that mixture momentum and energy equations can be employed. The present work focuses on flows where such homogeneous mixture approximations are not valid and full multi-fluid modeling is appropriate. In this approach, separate equations for the transport and generation of mass, momentum, and energy for each constituent are solved.

In the past two decades, two principal classes of algorithms have been developed for the solution of full multi-fluid systems. The first of these is derived from the implicit-continuous-fluid-Eulerian (ICE) method and involves a coupled or semi-coupled time-marching solution procedure [1–3]. These methods have found wide use in transient applications in the area of nuclear reactor safety. The second class of methods is the multi-field extension [5–7] of pressure-based schemes, widely used for single-phase applications [8]. These methods are segregated schemes that employ an iterative solution strategy along with under-relaxation. They have also enjoyed widespread use within the multi-fluid community.

In spite of their relative successes, both classes of schemes encounter some specific numerical difficulties in multi-fluid computations. It is well recognized that the single-pressure full multi-fluid time-marching system is non-hyperbolic in a strict sense because the eigenvalues of the inviscid differential system are complex for system parameters (e.g., volume fraction, slip) of practical interest [3, for example]. This raises issues regarding the stability of transient multi-fluid methods as well as the formulation of characteristic-based upwind discretization schemes. Pressure-based methods, on the other hand, are not based upon the unsteady system and, therefore, do not appear to suffer from the same problems. (It should be pointed out that this has been the source of some controversy within the research community.) However, the segregated procedures conventionally used in the pressure-based methods cause stability and robustness problems because the inter-phasic coupling terms cannot be treated in fully implicit fashion. This issue can be especially troubling when interfacial force models are non-linear in form and/or large in magnitude [7, for example]. Consistent with these observations, the overall objective of this work has been to develop a class of implicit schemes for full multi-fluid computations, which are both well posed and fully coupled.

The focus of this work is on obtaining steady-state solutions of full multi-fluid systems. Accordingly, the time-marching or relaxation procedure used serves merely as an iterative device to drive the solution errors to zero. Over the past decade, preconditioned time-marching methods have become widely researched and used [9, for example]. These methods introduce artificial time derivatives which control the system eigenvalues and thereby optimize stability and convergence properties of the scheme. In the context of steady-state multi-fluid computations, the preconditioning technique introduces the interesting possibility of selecting the time derivatives such that the system remains hyperbolic and, therefore, well posed for time marching. The examination of this promising avenue is one of the objectives of the paper.

The paper is organized as follows. The theoretical development begins with the steady-state equations and the discretization framework previously developed in conjunction with the pressure-based, multi-fluid algorithm. We introduce two under-relaxation procedures, the first based on the individual scalar transport equations and the second based on the fully coupled vector system. It is shown that the two under-relaxation schemes correspond to preconditioning systems, which we refer to as scalar and block preconditioning systems, respectively.

A hierarchy of analytical and computational procedures, including von Neumann stability analysis, matrix stability analysis, and sample computations (using a full non-linear CFD code based on the method), are utilized to probe the stability and convergence properties of the implicit scheme. The results of the von Neumann and matrix stability theories are restricted to the linearized version of the multi-fluid system. The von Neumann stability analysis further assumes the use of periodic boundary conditions. In spite of the limitations, the stability analyses provide rich insight into algorithmic performance. Indeed, these analyses serve as the guide for the selection of the optimal preconditioning system and solution procedure. Stability analyses are used to investigate the baseline performance of several candidate schemes. The effects of iterative method, preconditioning strategy, linearization strategy, and Reynolds number are investigated, and comparison to single-phase performance is presented. A hierarchy of increasing physical complexity is then pursued, starting with one-dimensional, two-fluid systems with minimum inter-field dynamic coupling and no mass transfer. These analyses are then extended to systems employing physically important inter-field forces (drag, dispersion, virtual mass). The effects of mass transfer, multiple fields (i.e., more than 2), and multiple dimensions are then considered.

Based upon the findings of these stability studies, a fully non-linear, multi-dimensional, multi-field code, COMAC, has been developed. Representative computational results obtained with COMAC which verify the stability findings and demonstrate the capabilites of the scheme under realistic operating conditions and practical boundary conditions are presented. In the interests of clarity, all the analyses and computations are performed for the one-dimensional system first, followed by more practical multi-dimensional results.

## THEORETICAL FORMULATION

### *Governing Equations*

In full multi-fluid formulations, independent equations are employed for the transport/generation of mass, momentum, and energy for each field present in a system. The ensemble averaged governing equations for steady-state, one-dimensional two-fluid flow without heat and mass transfer can be written as [10]

$$
\begin{aligned}
\frac{\partial}{\partial x}(\rho_1\alpha_1 u_1 u_1) &= -\alpha_1\frac{\partial p}{\partial x} + \frac{\partial}{\partial x}\left(\alpha_1\mu_1\frac{\partial u_1}{\partial x}\right)\\
\frac{\partial}{\partial x}(\rho_2\alpha_2 u_2 u_2) &= -\alpha_2\frac{\partial p}{\partial x} + \frac{\partial}{\partial x}\left(\alpha_2\mu_2\frac{\partial u_2}{\partial x}\right)\\
\frac{\partial}{\partial x}(\rho_1\alpha_1 u_1) &= 0\\
\frac{\partial}{\partial x}(\rho_2\alpha_2 u_2) &= 0\\
\alpha_1 + \alpha_2 &= 1,
\end{aligned}
\tag{1}
$$

where a conventional single-pressure approximation has been invoked. In what follows, each field's density and viscosity are assumed constant. For convenience, a factor of $4/3$ is assumed embedded within the molecular viscosities.

As written, Eq. (1) employs no dynamic coupling (e.g., drag) between fields 1 and 2, other than a common pressure. This model system serves as a platform for developing the implicit method presented below. The influence of dynamic coupling terms due to drag, virtual mass, and dispersion will be introduced. Also, the effects of mass transfer, alternate linearizations, multiple dimensions, and multiple fields on stability are investigated.

*Discretization*

Equation (1) is written in vector form as

$$
\begin{gathered}
R(Q) = \frac{\partial E}{\partial x} + \mathbf{B}\frac{\partial Q}{\partial x} + H = 0 \\
Q \equiv (u_1, u_2, \alpha_1, \alpha_2, p)^{\mathrm{T}}, \qquad H \equiv (0, 0, 0, 0, \alpha_1 + \alpha_2 - 1)^{\mathrm{T}} \\
E \equiv \begin{bmatrix} \rho_1\alpha_1 u_1 u_1 - \alpha_1\mu_1\dfrac{\partial u_1}{\partial x} \\ \rho_2\alpha_2 u_2 u_2 - \alpha_2\mu_2\dfrac{\partial u_2}{\partial x} \\ \rho_1\alpha_1 u_1 \\ \rho_2\alpha_2 u_2 \\ 0 \end{bmatrix}, \qquad \mathbf{B} \equiv \begin{bmatrix} 0 & 0 & 0 & 0 & \alpha_1 \\ 0 & 0 & 0 & 0 & \alpha_2 \\ 0 & 0 & 0 & 0 & 0 \\ 0 & 0 & 0 & 0 & 0 \\ 0 & 0 & 0 & 0 & 0 \end{bmatrix}.
\end{gathered} \tag{2}
$$

Several finite volume spatial discretization strategies can be applied. For the present work, second-order central differencing is selected for pressure gradient and viscous terms. First-order upwinding is used in conjunction with a conventional pressure-weighted interpolation scheme [11] for the convection terms in the momentum and continuity equations. Higher order accuracy can be employed straightforwardly, though for the purposes of the basic analyses presented in this paper only the stated discretization will be considered. Without loss of generality in the development which follows, $\Delta x$ is taken as constant, and $u$ is assumed positive.

Referring to Fig. 1, the discretization of Eq. (2) can be summarized as

$$
\begin{aligned}
\frac{\partial}{\partial x}(\alpha u u) &\rightarrow (E_{-x/2}\alpha)_{\mathrm{e}}(R_x u)_{\mathrm{e}}(E_{-x/2}u)_{\mathrm{e}} - (E_{-x/2}\alpha)_{\mathrm{w}}(R_x u)_{\mathrm{w}}(E_{-x/2}u)_{\mathrm{w}} \\
\frac{\partial}{\partial x}\left(\alpha\mu\frac{\partial u}{\partial x}\right) &\rightarrow \mu\overline{(\alpha)}_{\mathrm{e}}(\delta_x u)_{\mathrm{e}} - \mu\overline{(\alpha)}_{\mathrm{w}}(\delta_x u)_{\mathrm{w}} \\
\alpha\frac{\partial p}{\partial x} &\rightarrow \alpha_{\mathrm{P}}(\delta_{2x} p)_{\mathrm{P}} \\
\frac{\partial}{\partial x}(\alpha u) &\rightarrow (E_{-x/2}\alpha)_{\mathrm{e}}(R_x u)_{\mathrm{e}} - (E_{-x/2}\alpha)_{\mathrm{w}}(R_x u)_{\mathrm{w}},
\end{aligned} \tag{3}
$$

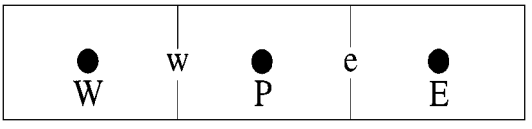


**FIG. 1.** 1-D control volumes on a Cartesian grid.

where the operators used in Eqs. (3) are defined as

$$\begin{aligned}(E_{-x/2}\phi)_{\mathrm{e}} &\equiv \phi_{\mathrm{P}}, \qquad \overline{(\phi)}_{\mathrm{e}} \equiv (\phi_{\mathrm{P}} + \phi_{\mathrm{E}})/2 \\ (\delta_x\phi)_{\mathrm{e}} &\equiv (\phi_{\mathrm{E}} - \phi_{\mathrm{P}})/\Delta x, \qquad (\delta_{2x}\phi)_{\mathrm{P}} \equiv (\phi_{\mathrm{E}} - \phi_{\mathrm{W}})/2\Delta x \\ (R_x u)_{\mathrm{e}} &\equiv \overline{(u)}_{\mathrm{e}} + \left(\frac{1}{\rho u/\Delta x + 2\mu/\Delta x^2}\right)[\overline{(\delta_{2x}p)}_{\mathrm{e}} - (\delta_x p)_{\mathrm{e}}].\end{aligned} \tag{4}$$

In Eq. (4), the second term on the RHS of the $R_x$ operator corresponds to the pressure-weighted interpolation [11].

*Implicit Solution Procedure*

Applying an exact Newton linearization to Eq. (2) yields

$$\mathbf{R}'(Q)\Delta Q = -R(Q), \tag{5}$$

where

$$\mathbf{R}'(Q) = \frac{\partial}{\partial x}\mathbf{A}\bullet + \frac{\partial}{\partial Q}\left(\mathbf{B}\frac{\partial Q}{\partial x}\right) + \mathbf{C}$$

and Jacobians

$$\mathbf{A} \equiv \frac{\partial E}{\partial Q}, \qquad \frac{\partial}{\partial Q}\left(\mathbf{B}\frac{\partial Q}{\partial x}\right), \qquad \mathbf{C} \equiv \frac{\partial H}{\partial Q}$$

are given in the Appendix.

The spatial discretization, given in Eqs. (3), is applied consistently on the RHS and LHS of Eq. (5). The fully implicit discrete linearized system becomes

$$\mathbf{P}Q^{n+1} = S(Q^n), \tag{6}$$

where, for notational simplicity in what follows, a non-$\Delta$ formulation is adopted. In Eq. (6), the block-banded matrix $\mathbf{P}$ (pentadiagonal with $5 \times 5$ blocks for 1-D, two-field) corresponds to the discretization of $\mathbf{R}'(Q^n)$, and $S(Q^n)$ corresponds to the discretization of $-R(Q^n) + \mathbf{R}'(Q^n)\bullet Q^n$. For completeness, vectors $\mathbf{P}Q^{n+1}$ and $S(Q^n)$ are given in the Appendix. The Newton scheme serves as a useful platform for investigating the effectiveness of solution strategies for solving the discrete system.

*General Iterative Solution*

A class of iterative schemes for the solution of Eq. (6) can be defined from

$$\mathbf{M}Q^{n+1,k+1} = \mathbf{N}Q^{n+1,k} + S(Q^n), \tag{7}$$

where

$$\mathbf{P} \equiv \mathbf{M} - \mathbf{N} \tag{8}$$

represents the iterative splitting adopted.

To facilitate discussion of the preconditioning and iterative strategies developed below, **P** can be decomposed as

$$\mathbf{P} = \mathbf{D} + (\mathbf{L} + \mathbf{U}), \tag{9}$$

where **D** is block diagonal, while **L** and **U** are strictly lower and upper block triangular. A decomposition of **D** is also introduced as

$$\mathbf{D} \equiv \mathbf{D}_\mathrm{d} + \mathbf{D}_\mathrm{o} + \mathbf{D}_\mathrm{c}, \tag{10}$$

where, for the linearization and discretization invoked, block diagonal matrix **D** is given in the Appendix and has the structure

$$\mathbf{D} = \mathrm{diag}\left\{ \begin{bmatrix} X & & X & & X \\ & X & & X & X \\ X & & X & & X \\ & X & & X & X \\ & & 1 & 1 & \end{bmatrix}, \begin{bmatrix} X & & X & & X \\ & X & & X & X \\ X & & X & & X \\ & X & & X & X \\ & & 1 & 1 & \end{bmatrix}, \ldots, \begin{bmatrix} X & & X & & X \\ & X & & X & X \\ X & & X & & X \\ & X & & X & X \\ & & 1 & 1 & \end{bmatrix} \right\}. \tag{11}$$

$\mathbf{D}_\mathrm{d}$ and $\mathbf{D}_\mathrm{o}$ correspond to diagonal and off-diagonal terms in rows 1–4 in each block of **D**. $\mathbf{D}_\mathrm{c}$ contains only the row 5 entries corresponding to the compatibility condition $\alpha_1 + \alpha_2 = 1$.

*Time-Marching and Relaxation Formulations*

Iterative procedures defined by Eq. (7) in general require some form of pseudo-time stepping or relaxation, to obtain stability and/or optimum damping. For example, the relaxation formulation conventionally used in segregated pressure-based schemes [8] may be expressed in vector form as

$$\left(\mathbf{M} + \mathbf{D}_\mathrm{d}\left(\frac{(1-\omega)}{\omega}\right)\right) Q^{k+1} = \mathbf{N}Q^k + S + \mathbf{D}_\mathrm{d}\frac{(1-\omega)}{\omega} Q^k. \tag{12}$$

Equation (12) can be written as an equivalent time-marching scheme,

$$\Gamma_\mathrm{S}\frac{\partial Q}{\partial t} + \mathbf{M}Q^{k+1} = \mathbf{N}Q^k + S, \tag{13}$$

by making the identification

$$\Gamma_\mathrm{S} = \mathbf{D}_\mathrm{d}\frac{(1-\omega)}{\omega}\Delta t. \tag{14}$$

Alternatively, a block-relaxation procedure may be defined:

$$\left(\mathbf{M} + \mathbf{D}\left(\frac{(1-\omega)}{\omega}\right)\right) Q^{k+1} = \mathbf{N}Q^k + S + \mathbf{D}\frac{(1-\omega)}{\omega} Q^k. \tag{15}$$

Equation (15) can be written as an equivalent time-marching scheme with block Jacobi preconditioning,

$$\Gamma_\mathrm{B}\frac{\partial Q}{\partial t} + \mathbf{M}Q^{k+1} = \mathbf{N}Q^k + S, \tag{16}$$

by making the identification

$$\Gamma_B = \mathbf{D}\frac{(1-\omega)}{\omega}\Delta t. \tag{17}$$

In practice, the algebraic compatibility condition $\sum \alpha_l = 1$ is enforced exactly. Accordingly, $\mathbf{D}$ is replaced by $\mathbf{D} - \mathbf{D}_c$ in Eqs. (15) and (17).

Equations (12)–(17) illustrate that relaxation formulations are closely related to time-marching solution methods. However, the form of the time derivatives in Eqs. (13) and (16) is different from the standard unsteady time derivatives used in conventional time-marching procedures [1–3]. Here, the time derivatives are "preconditioned" by the matrices $\Gamma_S$ and $\Gamma_B$. Accordingly, we refer to $\Gamma_S$ in Eq. (13) as the scalar preconditioning (or SP) matrix and to $\Gamma_B$ in Eq. (16) as the block preconditioning (or BP) matrix. The time-marching formulation is presented only for reasons of clarity. In the authors' flow solver, the time step is not directly specified; rather, the relaxation factor $\omega$ is specified and Eqs. (12) and (15) are implemented.

*Block Jacobi Scheme*

For a block Jacobi iteration,

$$\mathbf{M}_{BJ} \equiv \mathbf{D}, \qquad \mathbf{N}_{BJ} \equiv -(\mathbf{L}+\mathbf{U}). \tag{18}$$

When used with block Jacobi preconditioning, this scheme (hereafter designated BP-BJ) is written

$$\Gamma_B \frac{\partial Q}{\partial t} + \mathbf{D}Q^{k+1} = -(\mathbf{L}+\mathbf{U})Q^k + S. \tag{19}$$

A block Jacobi iteration with scalar relaxation (hereafter designated the SP-BJ scheme) is written

$$\Gamma_S \frac{\partial Q}{\partial t} + \mathbf{D}Q^{k+1} = -(\mathbf{L}+\mathbf{U})Q^k + S. \tag{20}$$

*Block Gauss–Siedel Scheme*

For a forward sweep block Gauss–Siedel scheme,

$$\mathbf{M}_{FBGS} \equiv \mathbf{D}+\mathbf{L}, \qquad \mathbf{N}_{FBGS} \equiv -\mathbf{U}. \tag{21}$$

Analogous to Eqs. (19) and (20), BP-BFGS and SP-BFGS schemes are defined:

$$\Gamma_B \frac{\partial Q}{\partial t} + (\mathbf{D}+\mathbf{L})Q^{k+1} = -\mathbf{U}Q^k + S \tag{22}$$

$$\Gamma_S \frac{\partial Q}{\partial t} + (\mathbf{D}+\mathbf{L})Q^{k+1} = -\mathbf{U}Q^k + S. \tag{23}$$

In practice the forward sweep block Gauss–Siedel schemes are used in conjunction with symmetric backward sweeps, defined analogously to Eqs. (22) and (23). These symmetric schemes are designated BP-BSGS and SP-BSGS, below.

## STABILITY ANALYSIS

Vector von Neumann analysis is employed to investigate the stability characteristics of the four preconditioned systems defined by Eqs. (19)–(20) and (22)–(23). These can be written in the common form

$$\mathbf{G}_1 Q^{k+1} = \mathbf{G}_2 Q^k + S. \tag{24}$$

The iteration matrix associated with the general scheme defined by Eq. (24) is

$$\mathbf{G} \equiv \mathbf{G}_1^{-1}\mathbf{G}_2. \tag{25}$$

The stability of the iterative schemes is assessed below by examining the eigenvalues of the Fourier symbol, $\hat{\mathbf{G}} = \hat{\mathbf{G}}_1^{-1}\hat{\mathbf{G}}_2$, of their iteration matrix, $\mathbf{G}$.

For a non-preconditioned, fully implicit scheme, $\hat{\mathbf{G}} = \hat{\mathbf{P}}$, where $\hat{\mathbf{P}}$ is the Fourier symbol of the matrix operator $\mathbf{P}$. For the schemes considered, $\hat{\mathbf{G}}_1$ and $\hat{\mathbf{G}}_2$ can be easily constructed by splitting $\hat{\mathbf{P}}$ appropriately (i.e., $\hat{\mathbf{P}} \equiv \hat{\mathbf{M}} - \hat{\mathbf{N}}$) and applying the preconditioning operators used.

There are eight physical parameters which appear in the system: cell Reynolds numbers associated with each phase ($\mathrm{Re}_1$, $\mathrm{Re}_2$), density ratio ($\rho_1/\rho_2$), velocity ratio ($u_1/u_2$), field 1 volume fraction ($\alpha_1$), and pressure and velocity gradient terms arising from the Newton linearization ($\delta_x u_1$, $\delta_{2x} p$). In what follows, stability characteristics are studied for the proposed iterative procedures applied to Eq. (6), for a range of physical parameters of interest.

*Block Jacobi Scheme*

The Fourier iteration matrix associated with the BP-BJ scheme defined in Eq. (19) is $\hat{\mathbf{G}}_{\text{BP-BJ}} = \hat{\mathbf{M}}_{\text{BP-BJ}}^{-1}\hat{\mathbf{N}}_{\text{BP-BJ}}$. For this scheme, the stability characteristics given in Fig. 2 are obtained. Here, the spectral radius of the amplification matrix for the BP-BJ scheme is plotted vs non-dimensional wave number.

The BP-BJ scheme is clearly conditionally stable for this case, where unity Reynolds numbers and zero pressure and velocity gradients were assumed. An optimum relaxation

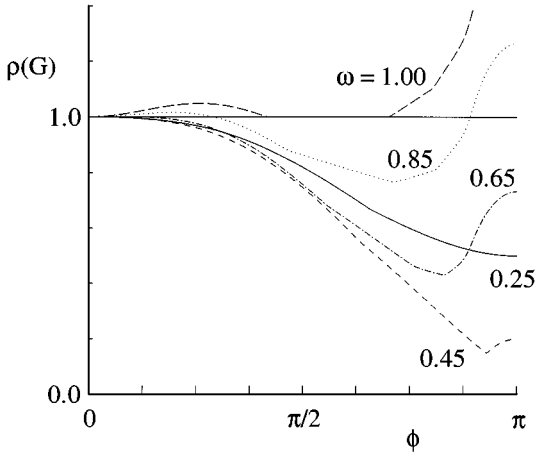


**FIG. 2.** Stability of the BP-BJ scheme.

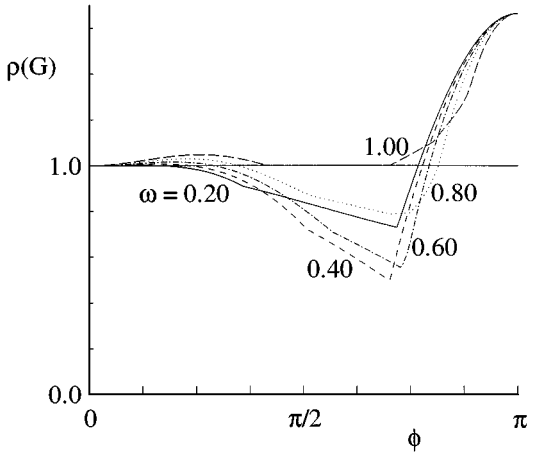


**FIG. 3.** Stability of the SP-BJ scheme.

factor of approximately $\omega = 0.45$ is observed, though this scheme exhibits significant stiffness at low wave numbers. The scheme is unstable for $\omega > 0.57$.

If scalar relaxation is used with the block Jacobi iteration (SP-BJ scheme defined by Eq. (20)), the stability characteristics shown in Fig. 3 are obtained. The SP-BJ scheme is observed to be unconditionally unstable.

*Block Gauss–Siedel Scheme*

Forward and backward block Gauss–Siedel schemes exhibit stability characteristics similar to block Jacobi. Specifically, both BP-BFGS and BP-BBGS schemes are conditionally stable, with $\omega_{\text{opt}} \cong 0.50$, and exhibit considerable low wave number stiffness. Also, both scalar preconditioned systems, SP-BFGS and SP-BBGS, are unconditionally unstable. For brevity, the stability plots for these four directionally biased schemes are not presented.

However, the construction of symmetric schemes from forward and backward block Gauss–Siedel component steps yields good damping properties. In Fig. 4, $\rho(\hat{\mathbf{G}}_{\text{BP-BSGS}})$, where $\hat{\mathbf{G}}_{\text{BP-BSGS}} = \hat{\mathbf{G}}_{\text{BP-BBGS}}\hat{\mathbf{G}}_{\text{BP-BFGS}}$, is plotted vs non-dimensional wave number. The

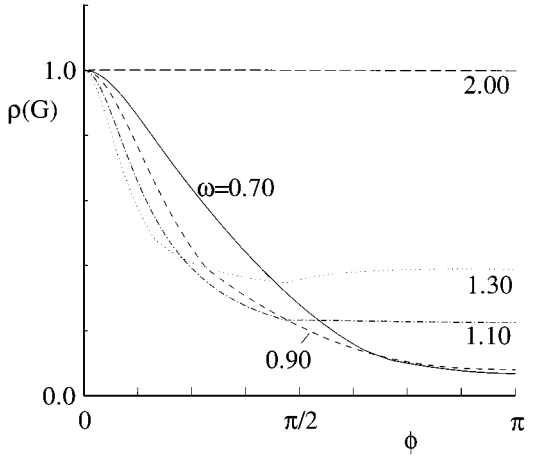


**FIG. 4.** Stability of the BP-BSGS scheme.

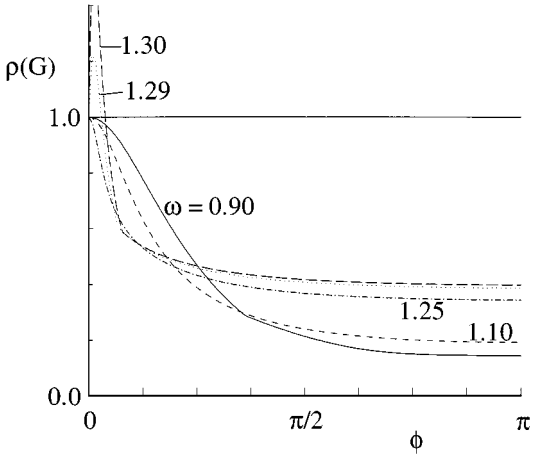


**FIG. 5.** Stability of the SP-BSGS scheme.

BP-BSGS scheme alleviates much of the low wave number stiffness associated with the BP-BJ scheme. Good damping is observed for $0.70 < \omega < 1.30$. Optimum low wave number damping is achieved for the 1-D scheme through over-relaxation, $\omega \cong 1.30$. Optimum high wave number damping, desired if a multi-grid procedure is to be employed, is achieved near $\omega \cong 0.90$. The BP-BSGS scheme remains stable to $\omega = 2.00$.

In Fig. 5, the stability for the SP-BSGS scheme is plotted. Unlike Jacobi and one-sided Gauss–Siedel iteration, scalar preconditioning does not yield an unconditionally unstable scheme when used with symmetric Gauss–Siedel iteration. Indeed, the damping characteristics of the SP-BSGS scheme are fairly good for $0.90 < \omega < 1.25$. However, the scheme is observed to become rapidly unstable at low wave numbers just above this range ($\omega_{\max} \cong 1.28$).

Of the four schemes investigated, BP-BSGS was chosen for further investigation, since it exhibits good damping properties and does not exhibit the potentially dangerous low wave number instability of SP-BSGS near its optimum damping range.

*Comparison with Single Phase*

The lack of inter-field transfer terms in the basic scheme defined by Eq. (1) renders the two fields dynamically uncoupled. Indeed, the model equation analyzed represents the independent response of the uncoupled phases to the same pressure distribution. Consistent with this observation, the multi-field stability results correspond closely to those obtained for the discrete single-phase analog to Eq. (1). In particular, the eigenvalues of the basic two-field system contain, as a subset, the eigenvalues arising in the single-field system.

To illustrate this, Fig. 6 shows an eigenvalue constellation for the BP-BSGS scheme ($\omega = 0.90$) applied to Eq. (6) with $\mathrm{Re}_1 = \mathrm{Re}_2 = 1.0$. A total of 21 modes ($-\pi < \phi < \pi$) were examined. At each of these wave numbers the two-field scheme returns four complex eigenvalues ($\lambda_5 = 0$, since compatibility is enforced without relaxation). The rank 2 single-phase system returns two complex eigenvalues. As seen in Fig. 6, these are equal to two of the four eigenvalues returned by the two-field system at the same wave number. The authors have observed (results not included for brevity) that the two new eigenvalues introduced in the two-fluid system can be limiting at low cell Reynolds numbers ($\mathrm{Re}_{1,2} < 1$), but the

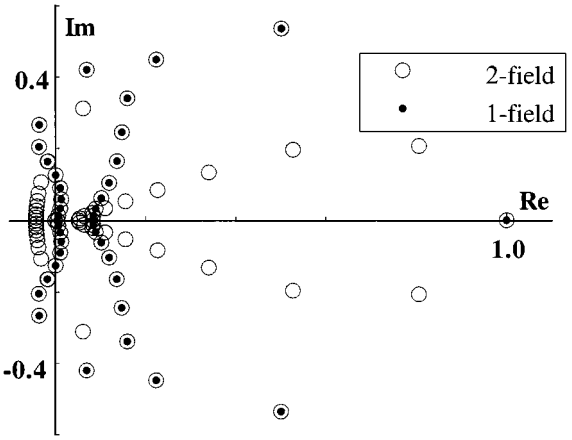


**FIG. 6.** Comparison of two-field eigenvalues to the one-field analog for the BP-BSGS scheme.

attendant increase in amplification factor is relatively small and is limited to low wave numbers.

*Frozen Coefficient Linearization*

It is necessary to maintain a full Newton linearization in the field continuity equations:

$$(\alpha u)^{n+1} \approx (\alpha^n u^{n+1}) + (u^n \alpha^{n+1}) - (u^n \alpha^n). \tag{26}$$

An alternative would be to lag the velocity in treating the volume fraction as a transported scalar, i.e., $(\alpha u)^{n+1} \approx (u^n \alpha^{n+1})$. This linearization choice is singular in the coupled scheme (on inspection of **D**).

On the other hand, such a "frozen coefficient" linearization may be employed for the convection terms in the momentum equations, i.e., $(\alpha u u)^{n+1} \approx (\alpha^n u^n u^{n+1})$. This is the approach that is conventionally utilized in pressure-based methods [7, 8]. Such a linearization choice has little or no effect on the linear performance of the coupled scheme. Indeed, for the particular discretization employed here, Eq. (3), such a frozen coefficient linearization has no effect on the stability of the basic scheme (in the absence of inter-field transfer terms). As illustrated below, however, the choice of frozen coefficient linearization in the momentum equations affects the overall (non-linear) convergence of the scheme.

## PARAMETRIC STUDIES

*Reynolds Number*

The effect of cell Reynolds number on stability can be assessed by parameterizing the Reynolds numbers for the constituent fields. Figure 7 shows the stability plots for the BP-BSGS scheme ($\omega = 0.90$) for a range of Reynolds numbers ($\mathrm{Re}_1 = \mathrm{Re}_2$) from $10^{-1}$ to $\infty$. Clearly the effect of the Reynolds number is a weak one, with only slightly deteriorated damping observed at infinite cell Reynolds numbers.

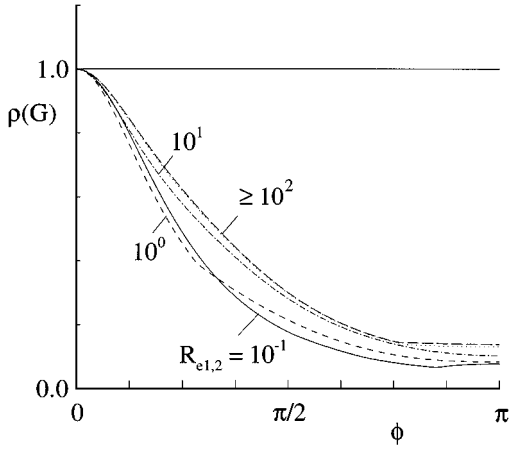


**FIG. 7.** BP-BSGS stability for a range of cell Reynolds numbers.

*Inter-field Transfer*

The introduction of interfacial dynamics and mass transfer couples the constituent fields. The impact of such terms on the physics of the flow and stability of the algorithm becomes dependent on the density ratio $(\rho_1/\rho_2)$, velocity ratio $(u_1/u_2)$, and field 1 volume fraction $(\alpha_1)$. Therefore, in order to meaningfully parameterize the stability of inter-field transfer terms, relevant engineering scales are adopted for these three flow parameters, and the field Reynolds numbers. In particular, for high-pressure steam–water boiling heat exchanger systems, the choices $\rho_1/\rho_2 = 10$, $u_2/u_1 = 1.5$, and $\alpha_1 = 0.5$ are relevant (hereafter designated HPW). For "bubbly" air–water flows, the choices $(\rho_1/\rho_2) = 1000$, $u_2/u_1 = 1.1$, and $\alpha_1 = 0.95$ are relevant (hereafter designated BAW). Typically, cell Reynolds numbers of $>10^3$ arise in practical engineering computations. The values $\mathrm{Re}_1 = \mathrm{Re}_2 = \infty$ are used below.

The most commonly employed models for interfacial momentum transfer are drag, dispersion, and virtual mass. The stability characteristics of these forces, and mass transfer, are treated below.

*Drag*

Drag is incorporated within the momentum equations as

$$\begin{aligned} \mathrm{M1} &\Rightarrow \mathrm{M1} + D \\ \mathrm{M2} &\Rightarrow \mathrm{M2} - D, \end{aligned} \tag{27}$$

where M1 and M2 denote the momentum equations in the baseline formulation (Eq. (1)). Drag, and all other interfacial transfer terms considered below, is consistently incorporated within the momentum equation interpolation procedure used for facial flux reconstruction [7] and, therefore, appear in the operator $R_x$ (Eq. (4)). Here, $D$ is modeled as [12]

$$D = \tfrac{1}{8} C_\mathrm{D} \rho_\mathrm{c} |u_1 - u_2| (u_2 - u_1) A_\mathrm{i}''', \tag{28}$$

where $C_\mathrm{D}$ is the drag coefficient, $\rho_\mathrm{c}$ is the "carrier" field density, and $A_\mathrm{i}'''$ is the interfacial area density. The assumed BAW and HPW scales are consistent with drag coefficients of $C_\mathrm{D} \cong 1.0$ and 0.1 respectively.

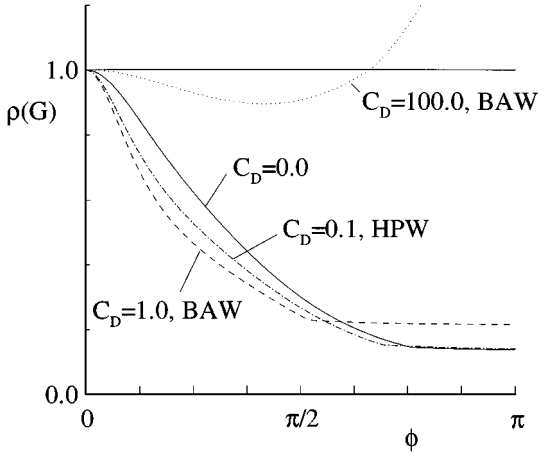


**FIG. 8.** BP-BSGS stability for a range of non-dimensional drag.

Figure 8 shows a comparison of the effect of drag on the damping properties of the BP-BSGS scheme ($\omega = 0.90$). In this plot, the two sets of physical scales introduced above (HPW, BAW) were specified, with $\mu_1 = \mu_2 = 0$ (inviscid). For physically reasonable magnitudes of $C_D$, the influence of drag on the linear stability of the scheme is small. However, extremely large values of drag (viz., unrealistic values as may occur in early iteration) are observed to destabilize the scheme, as shown in the figure.

*Mass Transfer*

Mass transfer is incorporated within the momentum and continuity equations as

$$\begin{aligned} \mathrm{M1} &\Rightarrow \mathrm{M1} + \Gamma^{21} u_2 - \Gamma^{12} u_1 \\ \mathrm{M2} &\Rightarrow \mathrm{M2} + \Gamma^{12} u_1 - \Gamma^{21} u_2 \\ \mathrm{C1} &\Rightarrow \mathrm{C1} + \Gamma^{21} - \Gamma^{12} \\ \mathrm{C2} &\Rightarrow \mathrm{C2} + \Gamma^{12} - \Gamma^{21}, \end{aligned} \tag{29}$$

where C1 and C2 denote the continuity equations in the baseline formulation (Eq. (1)). Here $\Gamma^{mn}$ are mass transfer rates from field $m$ to field $n$ in kg/m$^3$s, defined such that $\Gamma^{mn} \geq 0$. These terms are similar to drag, but are non-symmetric, and appear in the continuity equations. For $\Gamma^{mn} \approx \Gamma^{nm}$, the impact of mass transfer is similar to drag, so the non-symmetric cases are considered here. For the case where $\Gamma^{nm} = 0$, the maximum physically plausible value of $\Gamma^{mn}$ to be considered can be estimated from realizability constraints (i.e., $\alpha^{n+1} \geq 0$) to be

$$\Gamma^{mn^*} \equiv \frac{\Gamma^{mn}}{\rho_m \mathrm{u}_m \alpha_m / \Delta x} \leq 1. \tag{30}$$

Again, BP-BSGS is analyzed ($\omega = 0.90$). Small values of donor field volume fraction are taken ($\alpha_\mathrm{m} = 0.1$), consistent with proximity to the realizability limit. Other scales are taken as above (i.e., HPW, BAW, with $\mu_1 = \mu_2 = 0$ (inviscid analysis), $C_D = 0$). Figure 9 illustrates that values of $\Gamma^{mn^*}$ at the realizability limit do not significantly affect the linear stability of the scheme, though as with drag, very large values of mass transfer can be destabilizing.

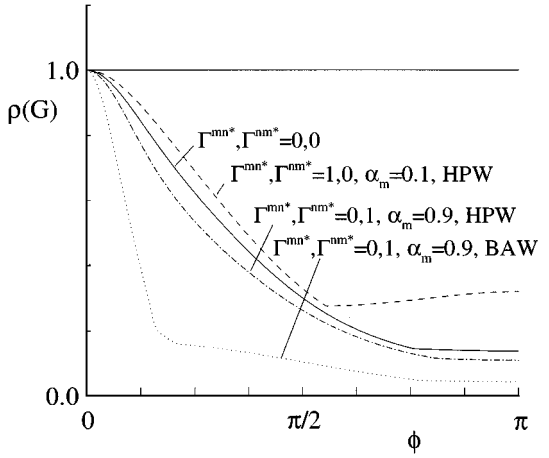


**FIG. 9.** BP-BSGS stability for a range of non-dimensional mass transfer.

*Dispersion*

Dispersion is incorporated within the momentum equations as

$$\begin{aligned} \mathrm{M1} &\Rightarrow \mathrm{M1} + C_{\mathrm{T}}\rho_1(u_2-u_1)^2\frac{\partial \alpha_2}{\partial x} \\ \mathrm{M1} &\Rightarrow \mathrm{M1} - C_{\mathrm{T}}\rho_1(u_2-u_1)^2\frac{\partial \alpha_2}{\partial x}. \end{aligned} \tag{31}$$

Physically reasonable values of the dispersion coefficient are $C_{\mathrm{T}} \leq 1.0$. As with drag and mass transfer, the influence of these terms on the stability of the linear scheme was found to be small (plot not included for brevity).

*Virtual Mass*

Virtual mass is incorporated within the momentum equations as

$$\begin{aligned} \mathrm{M1} &\Rightarrow \mathrm{M1} - C_{\mathrm{V}}\alpha_2\rho_1\left[u_1\frac{\partial u_1}{\partial x} - u_2\frac{\partial u_2}{\partial x}\right] \\ \mathrm{M2} &\Rightarrow \mathrm{M2} - C_{\mathrm{V}}\alpha_2\rho_1\left[u_2\frac{\partial u_2}{\partial x} - u_1\frac{\partial u_1}{\partial x}\right]. \end{aligned} \tag{32}$$

Considering the case of no mass transfer, Eq. (32) can be manipulated to yield modified effective convection terms in the two momentum equations:

$$\begin{aligned} \frac{\partial}{\partial x}(\rho_1\alpha_1u_1u_1) &\Rightarrow \left[1+C_{\mathrm{V}}\left(\frac{\alpha_2}{\alpha_1}\right)\right]\frac{\partial}{\partial x}(\rho_1\alpha_1u_1u_1) - \left[C_{\mathrm{V}}\left(\frac{\rho_1}{\rho_2}\right)\right]\frac{\partial}{\partial x}(\rho_2\alpha_2u_2u_2) \\ \frac{\partial}{\partial x}(\rho_2\alpha_2u_2u_2) &\Rightarrow \left[1+C_{\mathrm{V}}\left(\frac{\rho_1}{\rho_2}\right)\right]\frac{\partial}{\partial x}(\rho_2\alpha_2u_2u_2) - \left[C_{\mathrm{V}}\left(\frac{\alpha_2}{\alpha_1}\right)\right]\frac{\partial}{\partial x}(\rho_1\alpha_1u_1u_1). \end{aligned} \tag{33}$$

Physically reasonable values of the virtual mass coefficient are $C_{\mathrm{V}} \leq 0.5$. Figure 10 shows the impact of virtual mass on the stability of the BP-BSGS scheme ($\omega = 0.90$). Here the

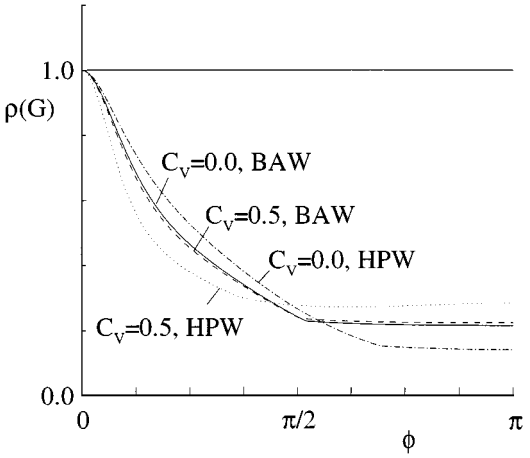


**FIG. 10.** BP-BSGS stability for a range of virtual mass coefficients.

BAW scales were run with $C_D = 1.0$ and the HPW scales were run with $C_D = 0.1$, as above. Linear stability is almost unaffected by virtual mass for the BAW scales, whereas a more noticeable but not significant impact is observed for the HPW scales.

## COMAC RESULTS—1-D

A two-dimensional, two-field Navier–Stokes code, designated COMAC, has been developed by the authors. This code is evolved from our earlier work, which is based on segregated pressure-based methodology [7]. Indeed, the spatial discretization employed in COMAC is the same as that used in the forerunner code. The ultimate goal of this work is to make COMAC a more robust and efficient analysis tool than its predecessor. The vector Fourier analysis presented above has been used to guide selection of the iterative and preconditioning scheme and linearization. To understand the effects of physical boundary conditions, and to verify the results of the vector analysis, matrix stability results for COMAC are included in this section. Sample convergence rates using the code applied in 1-D mode to a bubbly air–water flow are presented.

### *Comparison of Vector and Matrix Stability*

To illustrate the validity of the foregoing vector stability analyses, and to investigate the effect of physical boundary conditions on the scheme, a matrix stability analysis was performed. The platform for the matrix analysis is COMAC, using the BP-BSGS scheme introduced above.

A vertical air–water bubbly flow is investigated. Here, problem parameters were set at $\rho_1 = 1000$ kg/m$^3$, $\rho_2 = 1$ kg/m$^3$, $\mu_1 = 10^{-3}$ kg/ms, $\mu_2 = 10^{-5}$ kg/ms, $\Delta x = 0.05$ m, and ni = 20 (i.e., $L = 1.0$ m, 20 cells). A simple bubble drag model due to Wallis [13] was employed:

$$D = \frac{1}{8} C_D \rho_1 |u_2 - u_1|(u_2 - u_1)\frac{6\alpha_2}{D_b}, \qquad C_D \equiv \frac{6.3}{R_{eb}^{0.385}}, \qquad R_{eb} \equiv \frac{\rho_1 |u_2 - u_1| D_b}{\mu_1}. \quad (34)$$

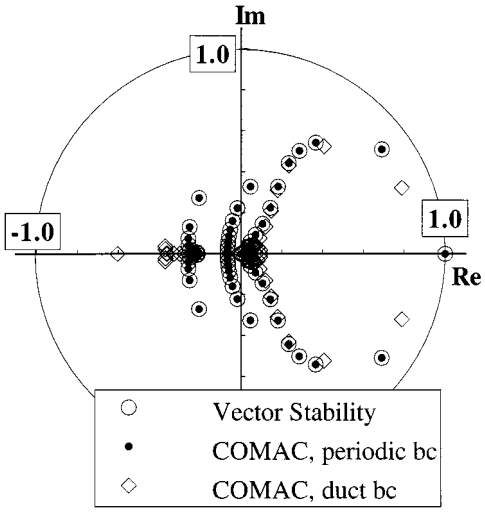


**FIG. 11.** Comparison of vector and matrix analyses for an air–water bubbly flow.

The flow solver's response to a given set of initial conditions, $u_1 = 1.0$ m/s, $u_2 = 1.1$ m/s, $\alpha_1 = 0.9$, and $\alpha_2 = 0.1$, was studied. A bubble radius of $D_b = 1.0$ mm was set. $\omega$ was set to 0.8 (Eq. (17)).

Figure 11 shows that if periodic boundary conditions are applied, COMAC returns iteration matrix eigenvalues which are coincident with those returned by the Fourier stability analysis. If conventional duct flow boundary conditions are applied (inlet: $u_1, u_2, \alpha_1$ fixed, $dp/dx = 0$; exit: $p$ fixed, $du_1/dx, du_2/dx, d\alpha_1/dx = 0$), the eigenvalue spectrum is modified as shown.

*Solver Performance*

Figure 12a shows linear solver convergence rates for the periodic and non-periodic COMAC runs at the first non-linear iteration (corresponding to Fig. 11). For this case, the

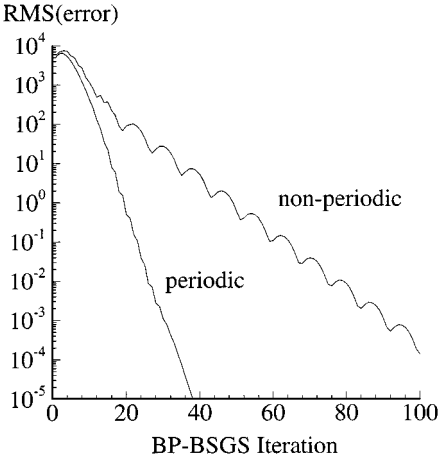


**FIG. 12a.** Comparison of BP-BSGS convergence histories for periodic and duct flow boundary conditions.

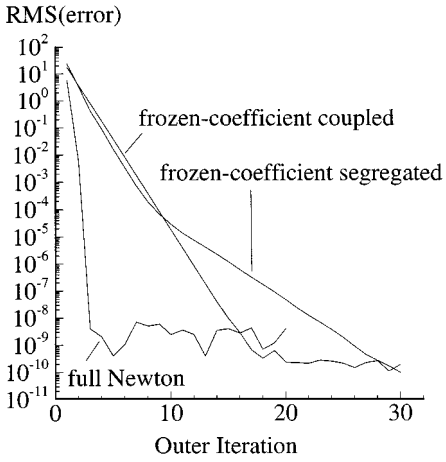


**FIG. 12b.** Comparison of full Newton and frozen coefficient linearizations on outer loop convergence.

application of physical boundary conditions are observed to deteriorate damping of the scheme somewhat. It is also noted that the physical boundary conditions considered reduce the stability limit for the scheme from $\omega = 2.00$ (refer to Fig. 4) to $\omega \cong 0.86$.

Figure 12b illustrates the outer (non-linear) convergence rates for this case. When a full Newton linearization is employed [drag (non-linear in $u_i$) and gravity linearized exactly], convergence to machine zero is obtained in four iterations. However, if a frozen coefficient linearization is utilized in the momentum equations, the convergence rate is significantly deteriorated. For comparison, the best obtainable convergence rates for this case were also obtained using the authors' predecessor segregated pressure-based code [7]. For this simple 1-D case the segregated method returns nearly as good a convergence rate as the frozen coefficient COMAC run.

The effects of mass transfer and under-relaxation factor on linear solver performance were investigated next. COMAC retains the two-fluid approach for the energy equations; that is, separate enthalpy equations are solved for each constituent field. Details of the implementation of the energy equations are beyond the scope of this paper, though they are fully coupled to the continuity, momentum, and compatibility equations, full Newton linearization is retained, and the block preconditioned iterative strategies employed are identical to those introduced above. A 1-D boiling vertical flow was computed. Problem parameters were set at $\rho_1 = 625\,\text{kg/m}^3$, $\rho_2 = 85\,\text{kg/m}^3$, $\mu_1 = 7.7 \times 10^{-5}\,\text{kg/ms}$, $\mu_2 = 2.4 \times 10^{-5}\,\text{kg/ms}$, $\Delta x = 0.05\,\text{m}$, and ni $= 20$ as above. Subcooled liquid is introduced at the inlet and volumetric heating is applied. After several non-linear iterations mass transfer is initiated (once the local temperatures exceed a critical value slightly above saturation temperture). Linear solver residual histories are presented for the BP-BSGS scheme in Fig. 13a for an outer loop iteration after mass transfer has begun. At this outer iteration the outlet vapor volume fraction is 0.2 and the outlet slip $u_2/u_1 = 1.1$. As expected, the convergence rate increases with increasing under-relaxation factor. The convergence rate is observed to deteriorate when $\omega$ is larger than approximately 0.75. Figure 13b shows similar plots for an adiabatic case adapted from the boiling flow just considered but with no heat/mass transfer and an inlet vapor volume fraction of 0.1. In comparing the two cases, it is apparent that the presence of mass transfer does not have a significant impact on the convergence of BP-BSGS. This is consistent with the stability analysis presented above which indicated that the presence of mass transfer does not adversely affect the amplification factors of the BP-BSGS scheme (see Fig. 9).

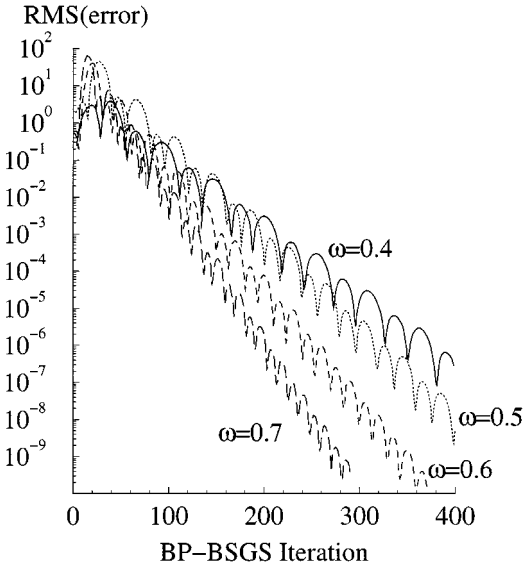


**FIG. 13a.** Comparison of BP-BSGS convergence histories for 1-D boiling flow computation for a range of relaxation parameters.

## EXTENSION OF STABILITY ANALYSIS TO MULTIPLE FIELDS

The analyses presented above for two fields extend readily to an arbitrary number of fields. As each new field is introduced to the basic scheme, two new eigenvalues appear, corresponding to the additional momentum and continuity equations. These two additional eigenvalues are identical to the two additional eigenvalues obtained in extending the

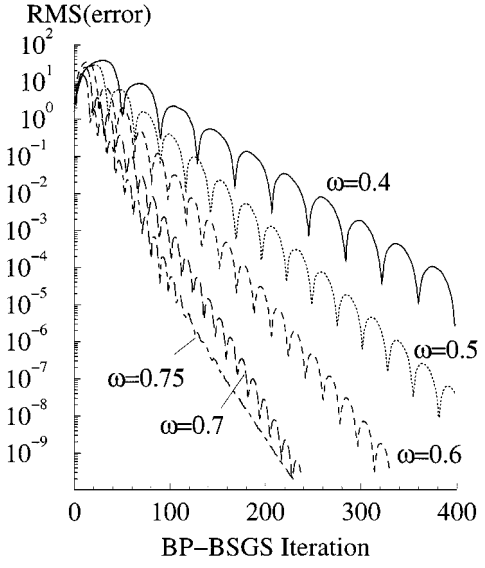


**FIG. 13b.** Comparison of BP-BSGS convergence histories for 1-D adiabatic flow computation with similar problem parameters as boiling flow in Fig. 13a.

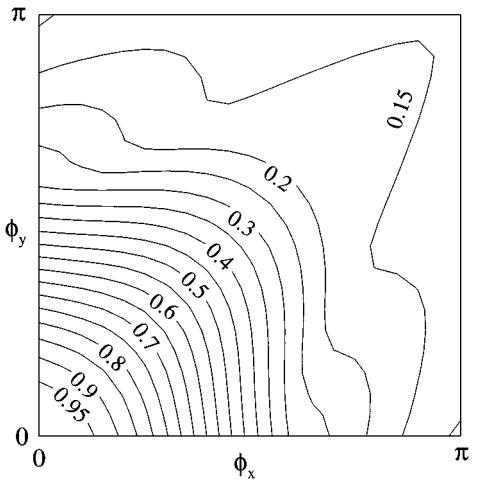


**FIG. 14a.** 2-D stability of the BP-BSGS scheme. AR $= u/v = 1$, $\omega = 0.80$.

single-field system to a two-field system. Accordingly, the $n$-field system exhibits stability characteristics identical to those of the two-field system.

## EXTENSION OF STABILITY ANALYSIS TO MULTIPLE DIMENSIONS

The stability analyses presented above for one dimension can also be readily extended to multiple dimensions. For two fields, the resulting Fourier eigensystem is of rank 7. Figure 14 shows examples of 2-D stability results obtained for the BP-BSGS scheme, with no interfacial transfer terms. Taking $u = v$, with $\mu_1 = \mu_2 = 0$ (inviscid), cell aspect ratio, AR $\equiv \Delta x/\Delta y = 1.0$, and $\omega = 0.80$, the results in Fig. 14a are obtained. There it is observed that the 2-D scheme exhibits good damping characteristics at all wave numbers away from the origin, consistent with the observations made above for the 1-D scheme. However, the 2-D scheme remains stable only to $\omega = 0.93$.

On high aspect ratio grids, as are characteristic of high $L/D_H$ boiling heat exchanger geometries, long wavelength axial modes become poorly damped as Fig. 14b illustrates.

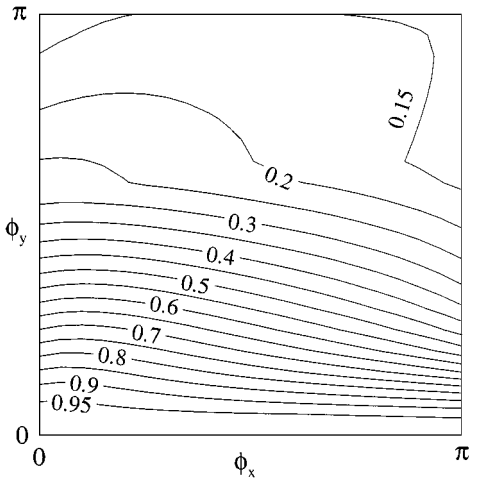


**FIG. 14b.** 2-D stability of the BP-BSGS scheme. AR $= u/v = 100$, $\omega = 0.80$.

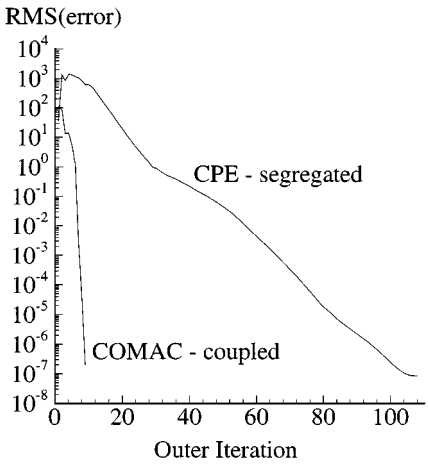


**FIG. 15.** Comparison of COMAC and segregated scheme outer loop convergence rates for a two-dimensional bubbly air–water vertical duct flow.

There a grid aspect ratio of 100 is assumed, $v$ is taken to be equal to $u/\mathrm{AR}$ ("well-guided" flow), and $\omega = 0.80$. Though the 2-D scheme remains stable to $\omega = 0.97$, long wavelength axial modes are very poorly damped. This low axial wave number stiffness is effectively handled by deploying a coupled block correction strategy, as discussed in [7].

## COMAC RESULTS—2-D

In order to demonstrate the validity of the 2-D stability results and the overall effectiveness of the algorithm for realistic multi-dimensional analysis, results of two sample computations performed with COMAC run in two-field, 2-D mode are presented in this section. The first simulation is of laminar air–water bubbly flow in a vertical duct. The liquid Reynolds

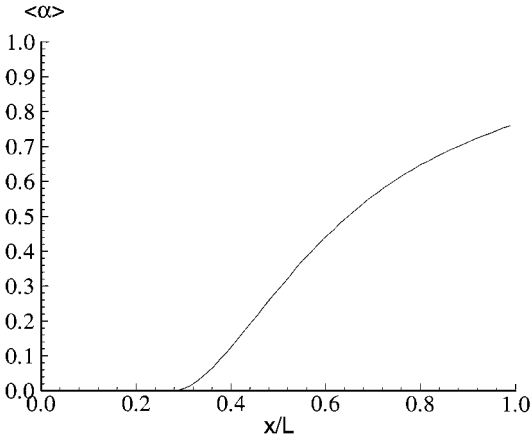


**FIG. 16a.** Predicted average volume fraction vs axial coordinate for a two-dimensional boiling turbulent steam–water vertical duct flow.

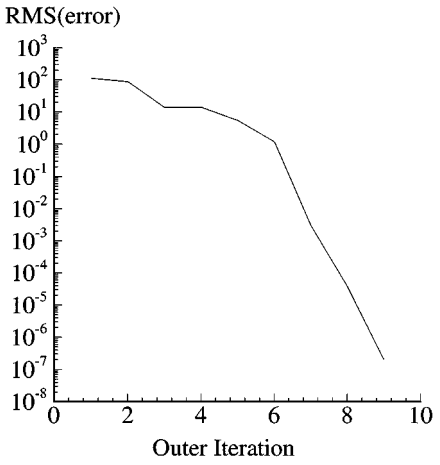


**FIG. 16b.** Outer loop convergence history for a two-dimensional boiling turbulent steam–water vertical duct flow.

number was 2332, and the density ratio was 858. Zero slip and an inlet vapor volume fraction of 0.10 were specified. The length to height ratio of the geometry was 6.0. A $64 \times 32$ mesh was employed. Figure 15 shows the outer loop convergence history for this computation using COMAC and its segregated algorithm-based predecessor. COMAC converges to machine zero in approximately 10 iterations, compared to over 100 for the segregated algorithm.

The second simulation is of turbulent boiling steam–water flow in a vertical duct. In this simulation, subcooled liquid enters a wall-heated vertical duct. Significant boiling is affected through mass transfer models based on wall heating and interfacial thermodynamics. A $64 \times 32$ mesh was employed. Figure 16a shows the predicted average steam volume fraction vs axial coordinate. Figure 16b shows the outer loop convergence history for this computation using COMAC. Because the Newton method is not, in general, globally convergent, a finite physical time step is introduced into the discretization for the first five iterations to maintain non-linear stability. At that point the physical time step is set to infinity, the Newton scheme is recovered, and the code exhibits Newton convergence to machine zero in another five iterations.

## CONCLUSION

An implicit method, developed for the solution of the viscous full multi-fluid equations, has been developed. Stability analyses were performed for preconditioned iterative schemes applied to the coupled discrete system of equations which arise in the formulation.

Several conclusions are drawn in the work, including the following: (1) A block symmetric Gauss–Siedel scheme with block Jacobi preconditioning (BP-BSGS) gives rise to good damping properties for the multi-fluid system. Good damping for the 1-D scheme can be obtained within a relaxation factor range of $0.8 < \omega < 1.5$. (2) A minimum level of exactness must be employed in developing an approximate Newton linearization for

the fully coupled system. An exact linearization in the momentum equations affords no benefit to the linear stability of the scheme compared to a "frozen" coefficient linearization, but can significantly improve the non-linear performance of the scheme. (3) In the absence of inter-field transfer terms, the basic multi-fluid scheme exhibits very similar stability characteristics to its single-phase analog. Only at very low cell Reynolds numbers does the multi-fluid system exhibit deteriorated damping properties compared to single phase. (4) Reynolds number effects are moderate; the limit of infinite cell Reynolds numbers marginalizes the stability of the scheme only slightly. (5) Implicit treatment of several interfacial transfer mechanisms investigated (mass transfer, drag, dispersion, and virtual mass) can affect the stability of the scheme, but the BP-BSGS scheme analyzed retains good damping characteristics for physically reasonable values of these modeled terms. (6) A multi-fluid Navier–Stokes code which deploys the BP-BSGS scheme has been developed. Comparison of vector and matrix stability verified the correctness of the vector analyses presented and demonstrated that physical boundary conditions can deteriorate the damping characteristics of the scheme. (7) The two-dimensional stability characteristics of the scheme are generally consistent with one-dimensional results, with high aspect ratio grids introducing diminished low wave number axial mode damping, as commonly observed in most CFD algorithms. However, the maximum stable relaxation factors for the BP-BSGS scheme drop from 2.00 in 1-D to approximately 0.95 in 2-D.

## APPENDIX

$$\mathbf{A} \equiv \frac{\partial E}{\partial Q} = \begin{bmatrix} 2\rho_1\alpha_1 u_1 - \mu_1\alpha_1\frac{\partial}{\partial x} & 0 & \rho_1 u_1 u_1 - \mu_1\frac{\partial u_1}{\partial x} & 0 & 0 \\ 0 & 2\rho_2\alpha_2 u_2 - \mu_2\alpha_2\frac{\partial}{\partial x} & 0 & \rho_2 u_2 u_2 - \mu_2\frac{\partial u_2}{\partial x} & 0 \\ \rho_1\alpha_1 & 0 & \rho_1 u_1 & 0 & 0 \\ 0 & \rho_2\alpha_2 & 0 & \rho_2 u_2 & 0 \\ 0 & 0 & 0 & 0 & 0 \end{bmatrix}$$

$$\frac{\partial}{\partial Q}\left(\mathbf{B}\frac{\partial Q}{\partial x}\right) = \begin{bmatrix} 0 & 0 & \frac{\partial p}{\partial x} & 0 & \alpha_1\frac{\partial}{\partial x}\bullet \\ 0 & 0 & 0 & \frac{\partial p}{\partial x} & \alpha_2\frac{\partial}{\partial x}\bullet \\ 0 & 0 & 0 & 0 & 0 \\ 0 & 0 & 0 & 0 & 0 \\ 0 & 0 & 0 & 0 & 0 \end{bmatrix}, \qquad \mathbf{C} \equiv \frac{\partial H}{\partial Q} = \begin{bmatrix} 0 & 0 & 0 & 0 & 0 \\ 0 & 0 & 0 & 0 & 0 \\ 0 & 0 & 0 & 0 & 0 \\ 0 & 0 & 0 & 0 & 0 \\ 0 & 0 & 1 & 1 & 0 \end{bmatrix} \quad \text{(A1)}$$

$$\mathbf{D} = \mathrm{diag}[\mathbf{D}_{ijk=1}, \mathbf{D}_{ijk=2}, \ldots, \mathbf{D}_{ijk=nijk}],$$

where

$$\mathbf{D}_{ijk} = \begin{bmatrix} \rho_1 E_{-x/2}\alpha_{1\mathrm{e}}^n R_x u_{1\mathrm{e}}^n + \frac{\rho_1}{2}\left[E_{-x/2}\alpha_1^n E_{-x/2}u_1^n\right]_{\mathrm{ew}} + \frac{\mu_1}{\Delta x}\left[\overline{\alpha_{1\mathrm{e}}^n} + \overline{\alpha_{1\mathrm{w}}^n}\right] & 0 & \rho_1 E_{-x/2}u_{1\mathrm{e}}^n R_x u_{1\mathrm{e}}^n - \frac{\mu_1}{2}\left[\delta_x u_1^n\right]_{\mathrm{ew}} + \Delta x \delta_{2x} p_{\mathrm{p}}^n & 0 & \frac{3\rho_1}{4\Delta x}\left[\kappa_1 E_{-x/2}\alpha_1^n E_{-x/2}u_1^n\right]_{\mathrm{ew}} \\ 0 & \rho_2 E_{-x/2}\alpha_{2\mathrm{e}}^n R_x u_{2\mathrm{e}}^n + \frac{\rho_2}{2}\left[E_{-x/2}\alpha_2^n E_{-x/2}u_2^n\right]_{\mathrm{ew}} + \frac{\mu_2}{\Delta x}\left[\overline{\alpha_{2\mathrm{e}}^n} + \overline{\alpha_{2\mathrm{w}}^n}\right] & 0 & \rho_2 E_{-x/2}u_{2\mathrm{e}}^n R_x u_{2\mathrm{e}}^n - \frac{\mu_2}{2}\left[\delta_x u_2^n\right]_{\mathrm{ew}} + \Delta x \delta_{2x} p_{\mathrm{p}}^n & \frac{3\rho_2}{4\Delta x}\left[\kappa_2 E_{-x/2}\alpha_2^n E_{-x/2}u_2^n\right]_{\mathrm{ew}} \\ \frac{\rho_1}{2}\left[E_{-x/2}\alpha_1^n\right]_{\mathrm{ew}} & 0 & \rho_1 R_x u_{1\mathrm{e}}^n & 0 & \frac{3\rho_1}{4\Delta x}\left[\kappa_1 E_{-x/2}\alpha_1^n\right]_{\mathrm{ew}} \\ 0 & \frac{\rho_2}{2}\left[E_{-x/2}\alpha_2^n\right]_{\mathrm{ew}} & 0 & \rho_2 R_x u_{2\mathrm{e}}^n & \frac{3\rho_2}{4\Delta x}\left[\kappa_2 E_{-x/2}\alpha_2^n\right]_{\mathrm{ew}} \\ 0 & 0 & 1 & 1 & 0 \end{bmatrix}$$

with

$$\kappa_{1\mathrm{f}} = \overline{\kappa_1}, \qquad \kappa_1 = 1 \Big/ \left[\frac{\rho_1 u_1}{\Delta x} + \frac{2\mu_1}{\Delta x^2}\right], \qquad \kappa_{2\mathrm{f}} = \overline{\kappa_2}, \qquad \kappa_2 = 1 \Big/ \left[\frac{\rho_2 u_2}{\Delta x} + \frac{2\mu_2}{\Delta x^2}\right].$$

## REFERENCES


1. D. R. Liles and W. H. Reed, A semi-implicit method for two-phase fluid dynamics, *J. Comput. Phys.* **26**, 390 (1978).
2. J. H. Mahaffy, A stability-enhancing two-step method for fluid flow calculations, *J. Comput. Phys.* **46**, 329 (1982).
3. H. B. Stewart and B. Wendroff, Two-phase flow: Models and methods, *J. Comput. Phys.* **56**, 363 (1984).
4. F. H. Harlow and A. A. Amsden, Numerical calculation of almost incompressible flow, *J. Comput. Phys.* **3**, 80 (1968).
5. D. B. Spalding, Mathematical methods in nuclear-reactor thermal hydraulics, Keynote Paper, ANS Meeting on Nuclear-Reactor Thermal Hydraulics, Saratoga, NY (1980).
6. R. I. Issa and P. J. Oliviera, Numerical prediction of phase separation in two-phase flow through T-junctions, *Comput. Fluids* **23**, No. 2, 347 (1994).
7. R. F. Kunz, B. W. Siebert, W. K. Cope, N. F. Foster, S. P. Antal, and S. M. Ettorre, A coupled phasic exchange algorithm for three-dimensional multi-field analysis of heated flows with mass transfer, *Comput. Fluids* **27**, No. 7, 741 (1998).
8. S. V. Patankar, *Numerical Heat Transfer and Fluid Flow* (Hemisphere, Washington, DC/New York, 1980).
9. Y. H. Choi and C. M. Merkle, The application of preconditioning to viscous flows, *J. Comput. Phys.* **105**, 207 (1993).
10. M. Ishii, *Thermo-Fluid Dynamic Theory of Two-Phase Flow* (Eyrolles, Paris, 1975).
11. C. M. Rhie and W. L. Chow, Numerical study of the turbulent flow past an airfoil with trailing edge separation, *AIAA J.* **21**, 1527 (1983).
12. R. T. Lahey, *Modern Developments and Advances in Boiling Heat Transfer* (Elsevier, Amsterdam/New York, 1992).
13. G. B. Wallis, *One Dimensional Two-Phase Flow* (McGraw–Hill, New York, 1969).